Anisotropic Transverse Confinement Design for Electrically Pumped 850 nm VCSELs Tuned by an Intra Cavity Liquid-Crystal Cell

Pierluigi Debernardi, Andrea Simaz, Alberto Tibaldi, Benjamin Boisnard, Thierry Camps, Francesco Bertazzi, Michele Goano, Benjamin Reig, Jean-Baptiste Doucet, Véronique Bardinal

Anisotropic Transverse Confinement Design for Electrically Pumped 850 nm VCSELs Tuned by an Intra Cavity Liquid-Crystal Cell

Pierluigi Debernardi, Andrea Simaz, Alberto Tibaldi, Benjamin Boisnard, Thierry Camps, Francesco Bertazzi, Michele Goano, Benjamin Reig, Jean-Baptiste Doucet, and Véronique Bardinal

Abstract

Relying on preliminary experiments, in this work we design a tunable 850 nm laser based on a hybrid combination of a liquid crystal micro-cell with nanoimprinted grating and an electrically-pumped GaAs half-VCSEL. The optical design is challenging due to the inherent tolerances of this hybrid technology, the presence of metals in the cavity and the need for single fundamental extraordinary mode emission over the whole tuning range. To ensure proper operation, we introduce for the first time the new concept of anisotropic transverse confinement design. The overall performance is verified by our multiphysics VCSEL suite. Beyond tuning features, we predict side mode suppression ratio and optical power under all working conditions, comparing the performance of liquid crystals with different clearing temperatures. The results qualifies these lasers as viable tunable sources with interesting performance and complementary features compared to other technologies.

Index Terms

Vertical cavity surface emitting lasers, Liquid crystal devices, Semiconductor lasers, Simulation.

I. Introduction

TUNABLE VCSELs are devices where wavelength is varied by changing the cavity optical length. Such components are very sought after, for several applications, ranging from datacom to sensing. Contrary to edge emitting tunable lasers, where the continuous tuning is limited to few nanometer, in VCSELs large tuning ranges can be achieved [1]. The state of the art in tunable VCSELs is represented by MEMS technology, where tuning is achieved by modifying the physical length of an air-gap in the tunable micro-electromechanical systems (MEMS) VCSEL [1], [2], [3]. Various tunable MEMS VCSELs have been demonstrated at 850 nm [3], [4] to 1550 nm [1] and up to 4 µm [5]. Quite remarkable is the first VCSEL operating at 1.06 µm in [6] for ophthalmologic optical coherent tomography systems. More recently, a tuning range of 37.7 nm with 76 V applied was reported at 850 nm [7]. This is the best tuning result at 850 nm to date.

However, MEMS might present drawbacks, such as relatively high tuning voltage and structural weakness that could make the moving part fragile. These devices could also be affected by ambient vibrations, which can alter their operation stability, or, at best, introduce strong extra noise.

As an alternative to MEMS, a promising novel approach is inserting a liquid crystal (LC) micro-cell as an intracavity layer of the VCSEL. In this case, the wavelength tuning is achieved by varying the refractive index of the LC, which modifies the cavity optical length.

Key advantages of this technology are large refractive index variations with moderate applied voltage, low power consumption and no moving parts.

The technology behind this idea is challenging, though, and no electrically pumped LC-VCSEL has been demonstrated so far. In fact, the need of creating an intracavity reservoir to host the LC is an additional difficulty compared to the MEMS approach. Experimental data are available for VCSELs, overlayed by an LC reservoir [8], [9], [10], which is very different compared to an intracavity tunable device.

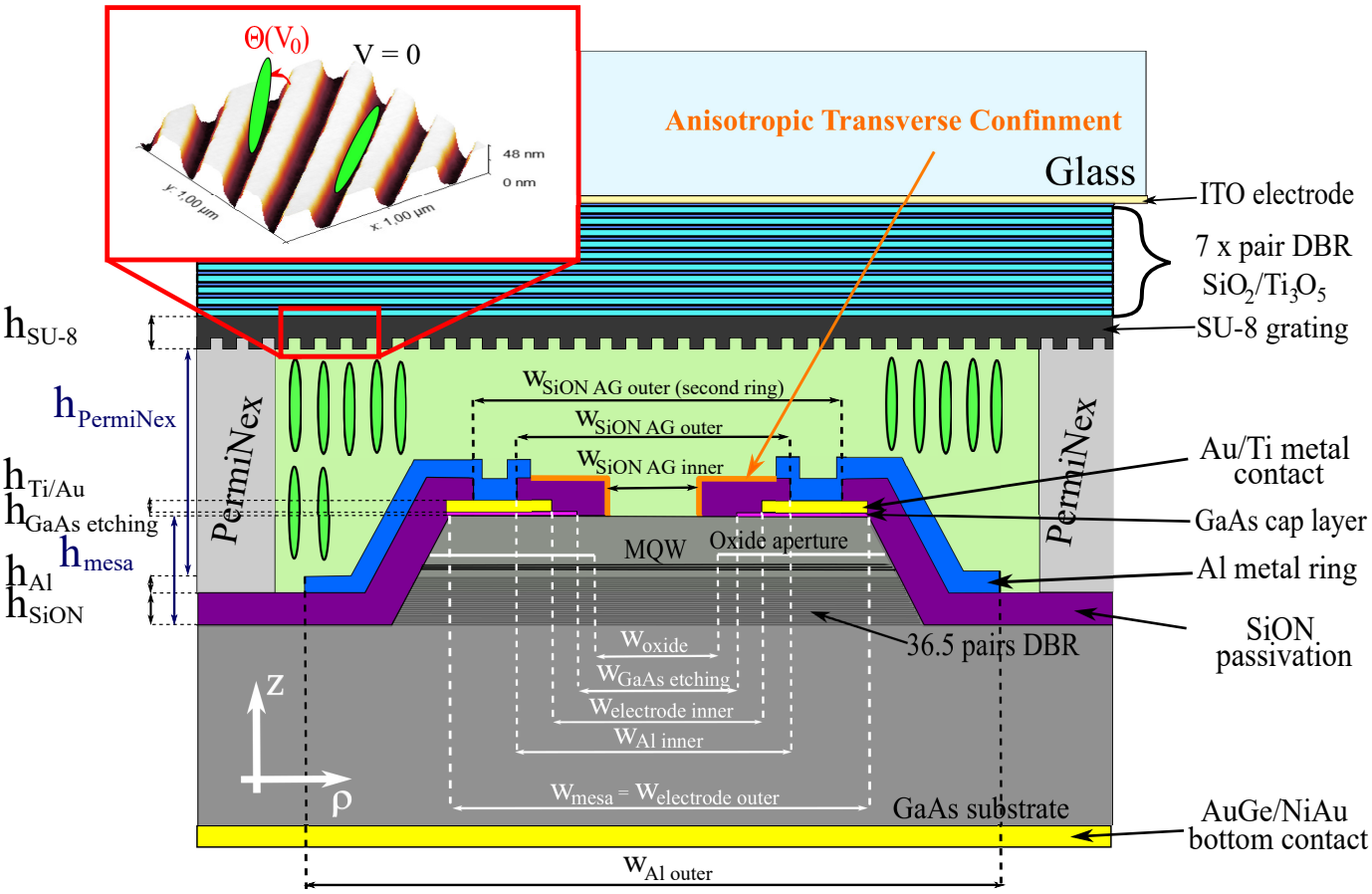

Fig. 1. ρ-z section of our hybrid LC tunable VCSEL. At top left an AFM image of the alignment grating, with a sketch of the molecule tilting governing the tuning mechanism. The LC molecules are represented by sticks, aligned to the grating at equilibrium. By applying voltage the molecules tilt toward $\hat{z}$, so that the LC becomes isotropic. An orange contour highlights the dielectric ring on which relies the anisotropic transverse confinement.

Hitherto two different approaches have been proposed: wafer fusion [11], [12] and hybrid approach [13], [14], both lacking experimental demonstration of an electrically driven device.

C. Belmonte et al. presented in 2015 a theoretical study of a 1.3 µm electrically driven LC-VCSEL that highlighted a thermal limitation at 50 °C using E7 [11]. More recently, the same group published further model details. In this approach, the thin azo-dye layers proposed for insuring LC alignment inside the cavity [15] are not compliant with the high-temperature needed for wafer fusion [16]. Wafer-fusion technology itself has never entered mass production, which points to inherent criticalities.

Our approach is mainly based on the use of polymers for the LC cell fabrication. The general advantages of organic materials, as compared to inorganic compounds, are numerous: energy saving and thermal compatibility due to requirement of temperatures below 200 °C for the process, no need of costly and heavy equipment, as well as a variety of possible materials to be used. Most of all, our approach seems a bit more mature because different intermediate steps of the technology have been already demonstrated. The use of a single SU-8 nanograting for LC alignment and of polymer-based walls to define the LC microcells made indeed the fabrication of first efficient tunable optical devices possible, like passive Fabry-Pérot filters [17], tunable III-V photodiodes (with electrodes and microreliefs) [18]. More recently, optically-pumped 1.55 µm VCSELs [14] were demonstrated within our technology, displaying a continuous tuning of about 23.5 nm in CW.

To guide the experimental work and make it more effective, we design here an electrically-driven 850 nm LC-VCSEL. It is based on the same tunable section adopted in the successful device reported in [14], which solves issues directly related to our hybrid technology. At the same time, we investigate the

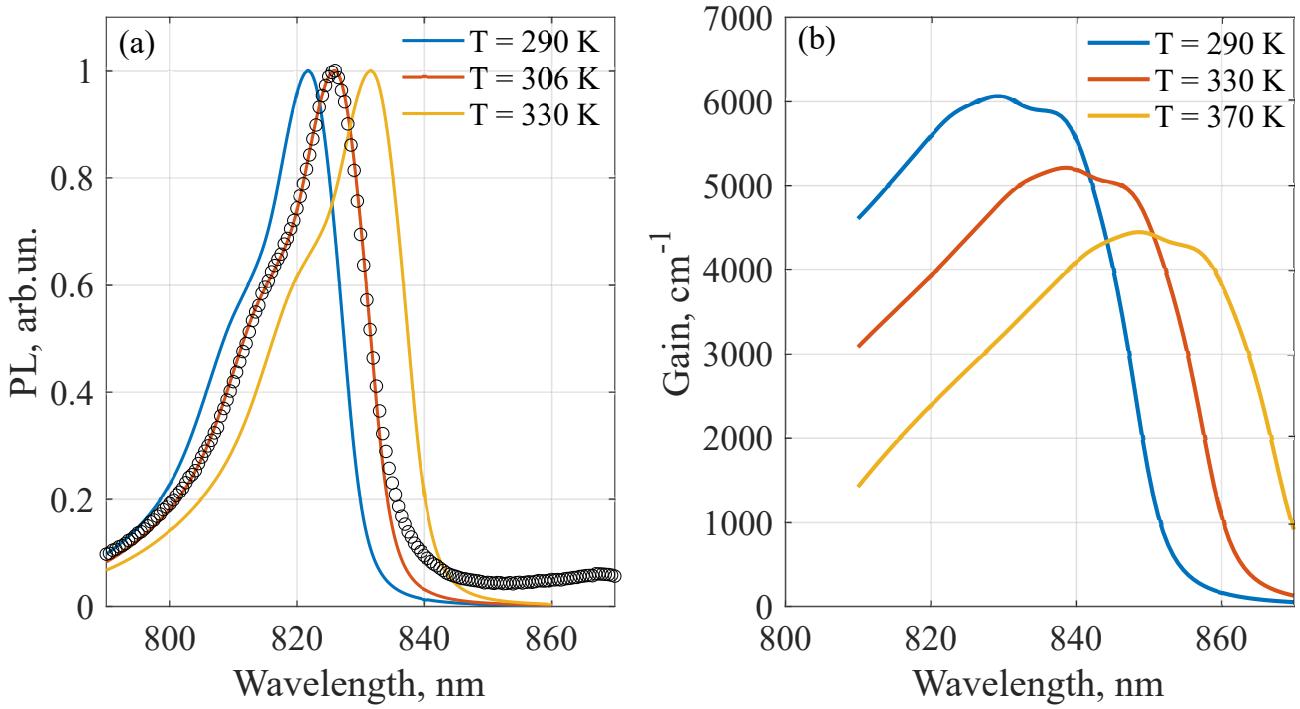

Fig. 2. (a): photoluminescence (PL) spectra at different temperatures; open black circles refer to the measured PL of a test sample. (b): gain spectra for different temperatures at $n = p$=6 $\times$ 10^{-12} cm^{-2}.

relevant transverse effects and the issues related to electrical injection in the 850 nm half-VCSEL. Since the two methods used for the fabrication of the LC microcell's walls, inorganic and organic, differ so much, the related issues are totally different and, correspondingly, their designs. Therefore this requires vectorial optical simulations of a complex structure including anisotropic layers, accounting for thermally induced variations of refractive indices, very important in these devices for the antiguiding features of LCs [12].

In Section II we present the structure and the technology driven constraints which influence our electrical and optical designs. They guide our electrical and optical designs. As a first step, in Section III we carry out detailed 1D optical simulations and we introduce for the first time our anisotropic transverse confinement design to suppress ordinary mode lasing. The entire structure is then validated to cope with the various guiding/antiguiding issues and to assure proper tuning operation. With this aim, we use VELM (Vcsel ELectroMagnetic) [19], [20], [21], our vectorial optical solver, in its standalone version, capable to include also the effects of the LC-alignment grating [22]. After obtaining an optimal optical design, in Section IV we cross-check its performance against operation. To that end, we deploy our computer-aided multiphysic software for circularly symmetric VCSEL analysis [23]. In this way we can investigate the above threshold modal features and their dependence on current (fundamental mode operation and side-mode suppression ratio, SMSR), capability of the quantum well (QW) gain to sustain lasing over the whole free spectral range (FSR, the distance between two longitudinal modes), and optical power performance vs. tuning and oxide apertures.

II. Structure and first experimantal steps

The hybrid structure considered in this study is sketched in Fig. 1 and composed of 3 main parts: an electrically-pumped half-VCSEL device (bottom, in grey), a polymer-based microcell containing the LC (center, in green) and a dielectric top mirror including a LC alignment grating, which seals the LC reservoir (top part in Fig. 1).

A. Half VCSEL

The GaAs half-VCSEL, similar to the one used by Kögel *et al.* for 850 nm tunable MEMS-VCSEL fabrication [3], comprises a bottom *n*-type distribuited Bragg reflector (DBR) made of 36.5 pairs of ($Al_{0.85}Ga_{0.15}As/Al_{0.1}Ga_{0.9}As$) with graded interfaces to improve current injection [24], an undoped active MQW region with 3 GaAs 6 nm-thick QWs separated by 8 nm-thick $Al_{0.3}Ga_{0.7}As$ barriers. The QW design is even more important than in standard devices. In fact, in tunable VCSELs the whole resonator free spectral range must match the optical gain response. In Fig. 2 we report the PL of a preliminary grown QW region, compared with our QW optical model [23], showing a good match between model and experiment. At right we show computed gain spectra in the working temperature range, which is compliant with the wavelength performance of our structure (825-50 nm, see Fig. 6).

Above the active region, the structure is terminated by an upper *p*-doped spreading layer ($Al_{0.85}Ga_{0.15}As$), covered by a 90 nm-thick highly *p*-doped GaAs cap-layer for good ohmic contact with the metal contact ring. As in MEMS-VCSEL devices, this layer has to be locally etched from the device center, because its absorption of $\approx 10\,000\,cm^{-1}$ would prevent laser action. This is a more critical situation than in standard AlGaAs VCSELs, where this layer is at the end of the *p*-DBR.

After the fabrication of a top annular Ti/Au p-contact-ring (in yellow in Fig. 1) and a full plate bottom *n*-type contact, 36 µm circular mesas are defined by dry etching of the multilayer stack up to the *n*-doped area giving access to the $Al_{0.98}Ga_{0.02}As$ layer that will be oxidized in high temperature water-vapour. The resulting oxide aperture provides current and optical confinement at the same time. A SiON dielectric layer is used for device passivation and to act as a guiding/antiguiding ring to enable tuning operation (see Sec. III-C). An aluminium (Al) contact pad is finally deposited to insure a deported electrical access for each device after LC microcell integration.

B. LC Reservoir and Top DBR

The grating+DBR section is supported by polymer walls, whose self-sealing properties are exploited for the final device assembly at the end of the fabrication process. The third part is a dielectric DBR made of $7x(SiO_2/Ti_3O_5)$ pairs deposited on a 0.7 µm-thick glass substrate having a 45 nm-thick transparent conductive ITO electrode on its surface. A thin SU-8 layer, a negative photoresist, is deposited on the surface of this mirror and a 200 nm-period polymer grating that will serve for LC alignment is fabricated by nanoimprint lithography (NIL) in the SU-8 layer (grating depth 48 nm, duty cycle 50%) [17]. The process used here is similar to the one reported by the authors for the fabrication of optically-pumped LC tunable VCSELs [14]. The cells are collectively assembled by thermal sealing under pressure of the (glass/ITO/DBR/grating) stack placed upside down above the PermiNex walls.

For the top dielectric DBR, the choice of 7 pairs is determined by observing that down to 8 pairs threshold does not change (it is determined by the free carrier absorption in the spreading layer), while 6 pairs result in a much higher threshold, which would compromise the overall device performance [25].

C. Liquid Crystals

The used nematic LC consists of electro-sensitive molecules, which are sketched in light green in Fig. 1. As indicated in this picture, their shape is rod-like. Treating the LC as an effective medium, these elongated shapes cause light propagation in the LC to be anisotropic. At equilibrium, the LC molecules are aligned to the grating lines, see top-left inset of Fig. 1. In this condition, the optical anisotropy or birefringence is maximum and we define as n_e the extraordinary index (in the direction of the grating lines) and n_o the ordinary one (perpendicular to the grating grooves). By applying the tuning voltage the molecules orientation is modified, making the extraordinary index voltage-dependent. When the molecules become vertical, they exhibit a 1:1 aspect ratio, and the optical anisotropy fully disappears. These concepts are sketched in the inset of Fig. 1. The nematic LC material is introduced in the cells under vacuum and above its clearing temperature, where the anisotropy disappears. This corresponds to the temperature where the ordinary and the extraordinary branch meet (see Fig. 2 of [26]).

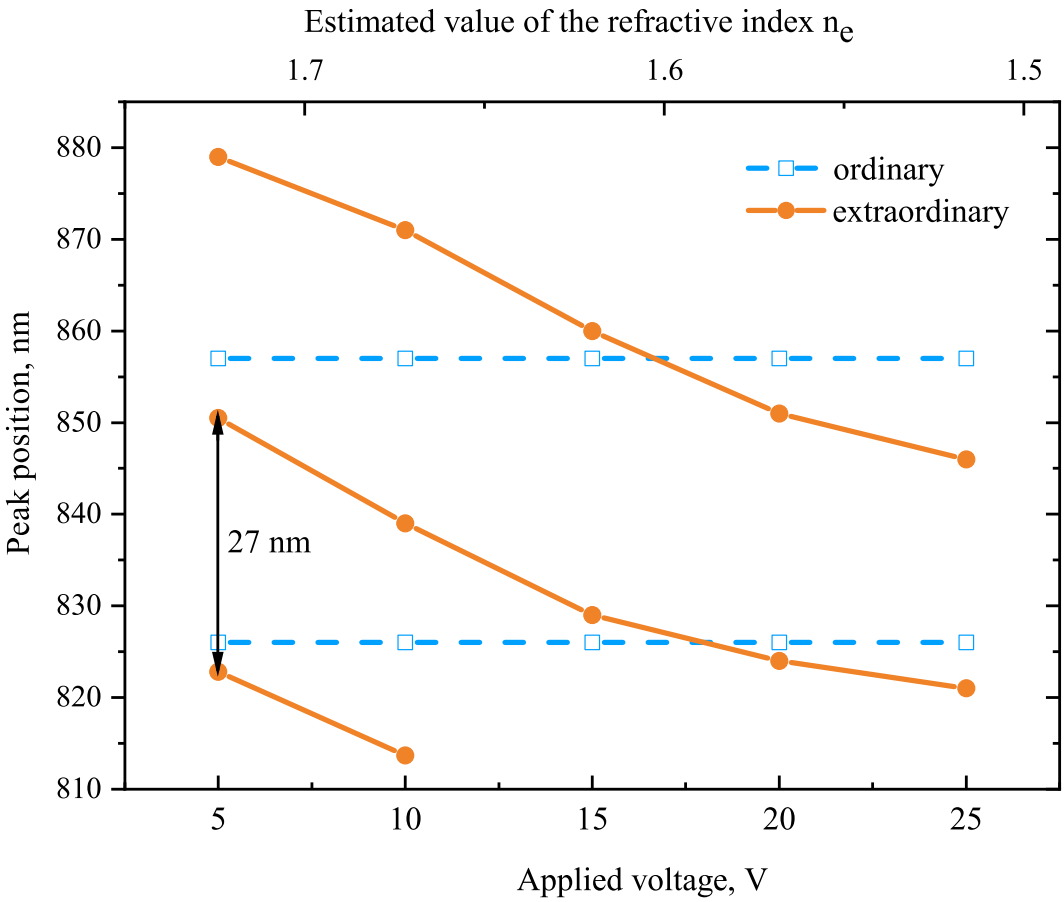

Fig. 3. Measurement of the spectral positions of the ordinary (blue) and extraordinary (red) mode positions as a function of the applied voltage for a test sample with a LC-microcell integrated on a non-electrically processed half-VCSEL. Only the voltage range above the LC threshold (5 V) is shown. The estimated variation of the refractive index n_e is reported on the top axis.

Two types of LC are investigated in this work: type 1 (QYPDLC-07 from QingDao, similar to standard E7 from Merck) and type 2 (QYPDLC-036). Both exhibit a significant birefringence at room temperature: n_e-n_o= 0.227 and 0.253 respectively. The latter displays superior temperature features, i.e. its clearing temperature is higher: 368 K, compared to 331.6 K. The thermal decrease of the refractive indexes below the clearing temperarure is inferred from the litterature [26] and from a complementary study [27]. LC absorption is almost negligible in the NIR range and we used the literature value of 0.08 cm^{-1} at 850 nm [28].

D. Experiments for FSR and LC-cell tuning features

In Fig. 3, we check the tuning capability of our LC technology at 850 nm, using a simpler LC-structure directly integrated on a non-processed III-V epilayer, with no electrical injection features. In this way, the reflectance spectrum can be easily measured by FTIR spectroscopy inside the LC micro-cell on a flat and large surface (≈400 μm^2). In this intermediate device, the LC reservoir height is equal to that of PermiNex wall and estimated to be 2600 nm and the etching depth is about 120 nm (90 nm of the GaAs cap layer + 30 nm in the layer below). The spectral position of the resonances of the reflectance spectrum is measured varying the applied voltage. As observed in Fig. 3, the extraordinary modes positions can be tuned above 5 V applied, whereas the ordinary modes positions remain unchanged whatever the applied voltage, as expected. This preliminary result shows the scalability of our technology and indicates its feasibility at 850 nm.

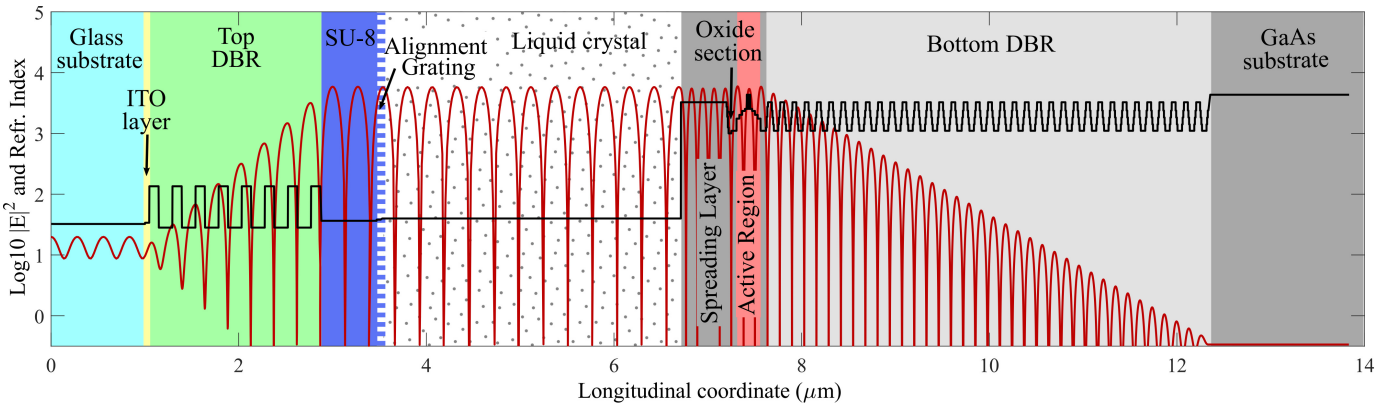

Fig. 4. 1D optical standing wave (red, λ=841 nm, G_{th}=631 cm^{-1}) and corresponding longitudinal refractive index profile (black) for n_e=1.60, SU-8=0.6 µm, h_{LC}=3 µm. The various sections have emphasized with different colors.

E. Geometrical Constraints and Tolerances

All the geometrical dimensions and technological tolerances are detailed in Table I. Taking into account these variations, the resulting LC thickness at the device center can be expressed as:

$$h_{LC} = h_{PermiNex} - h_{mesa} + h_{GaAs} + h_{SiON} \quad (1)$$

TABLE I
KEY PARAMETERS, DESIGN VALUES WITH THEIR UNCERTAINTIES AND THEIR TECHNOLOGICALLY FEASIBLE RANGES (MIN/MAX); ALL SIZES ARE IN μm.

Parameter	**Symbol**	**Design & Tol.**
Alignment grating SU-8 layer thickness	h_{SU-8}	0.6 ± 0.1
Polymer microcell: PermiNex wall height	$h_{PermiNex}$	3.50 ± 0.05
Half-VCSEL Antiguiding ring height	h_{SiON}	1.00 ± 0.05
Antiguiding ring (AG) inner diameter	$w_{SiON\ AG\ inner}$	6 ± 1
AG outer diameter	$w_{SiON\ AG\ outer}$	14 ± 1
AG second ring		30 ± 1
Ti/Au electrode inner diameter	$w_{electrode\ inner}$	12 ± 1
Al contact pad: inner diameter	$w_{Al\ inner}$	14 ± 1
Al contact pad: outer diameter	$w_{Al\ outer}$	50 ± 1
Mesa height	h_{mesa}	1.30 ± 0.15
Mesa diameter	w_{mesa}	36 ± 1
Oxide aperture diameter	w_{oxide}	4 ± 1
GaAs local etching diameter	$w_{GaAs\ etching}$	6 ± 1
GaAs local etching depth	$h_{GaAs\ etching}$	0.10 ± 0.01

which means that its tolerance is mainly given by h_{mesa} and h_{PermiNex}, i.e. $\pm$200 nm, as the uncertainties on the other layers can be neglected. The key parameter h_{PermiNex} can be varied between 3 µm and 5 µm by playing on spin-coating conditions during wall fabrication.

The thickness of the SiON layer plays also a significant role: the higher the h_{SiON}, the higher the anysotropic guiding effect (Section IV-C). However, for LC filling considerations, the LC channel height should be not lower than 0.5 µm at any location on the sample. Consequently, the maximal value for h_{SiON} is 1 µm. In these conditions, depending on the chosen PermiNex height, h_{LC} can be set between 2.3 µm and 4.8 µm. Due to uncertainties on the PermiNex thickness during its deposition by spin coating (2.6%), h_{LC} cannot be controlled with a precision better than $\pm$50 nm. Additionally, the thickness of the thin SU-8 layer used for the fabrication of the LC alignment grating on the DBR/glass substrate cannot be controlled with a precision better than $\pm$100 nm (14%). These significant uncertainties have to be taken into account in the optical design.

III. Optical Analysis

The tuning features can be investigated by a simple one-dimensional (1D) analysis of the axial (ρ=0) section of the device sketched in Fig. 1 and summarized in table II. The 1D simulations are performed by VELM-1D, where the effect of the LC alignment grating is introduced on the same footing as in VELM-3D. The grating is studied rigorously by RCWA approach [29]. The inferred properties are converted into transmission matrix, required by VELM. The code is run twice, for EM (extraordinary mode, TE, parallel to the grating grooves) and OM (ordinary mode, TM, orthogonal to the grating lines). As an example, in Fig. 4 we provide a standing wave profile for $n_e = 1.60$, superimposed to the refractive index profile, showing also the most relevant sections of the longitudinal optical resonator.

A. FSR and threshold gain

At first, we investigate the FSR (free spectral range) in Fig. 5 and the corresponding threshold gain vs. the etching depth of the semiconductor layer below the GaAs contact layer. This rules the phase conditions, making the design resonant (0 nm) or anti-resonant (60 nm) [3]. This means that the field displays an antinode/node at the semiconductor-LC interface. In the latter case, the interface is not seen by the field, which leads to a much higher threshold and a maximum FSR. In fact, this condition corresponds to a best superposition of the standing wave with the LC.

The cavity phase conditions allow a strong variation of the FSR, from about 20 to 40 nm, as shown in Fig. 5. This variation is accompanied with an important increase of the threshold gain, averaged over the tuning range (see Fig.5 (b)). From a minimum value of about 1000 cm^{-1}, threshold reaches values higher than 2500 cm^{-1}.

The LC thickness has a weaker impact on the FSR, which diminishes at increased values. We simulated two cases: minimum LC thickness in our technology, 2300 nm, and the targeted value of 3000 nm. The interval between two extraordinary modes (FSR) is about 27 nm in our test sample (Fig. 3), which is in good agreement with our 1D model, as shown with the green cross in Fig. 5 (a).

In our design we prefer to keep the threshold gain as low as possible, so the etching of this underlying layer is set to 10 nm, to be sure that the highly absorbing GaAs layer is fully removed. Moreover, the LC cell is targeted at 3000 nm, to ensure a good LC filling. This choice limits the achievable FSR to 23 nm, about half of the maximum value of 44 nm of an antiresonant design.

B. Tuning features

In a tunable LC-VCSEL we need to master several features at the same time. The device must lase on the fundamental transverse mode and with the (voltage-dependent) extraordinary polarization over the whole tuning range. These requirements are even more challenging within our technology. Being h_{LC} and $h_{\mathrm{SU-8}}$ uncertainties of the same order of the material wavelengths, they introduce large variations to

the round-trip phase shift. This might cause the (voltage-independent) ordinary mode to win against the extraordinary one, preventing the desired tuning operation.

The 1D geometry of Fig. 4 is investigated in Fig. 6, where a parametric investigation of the tuning characteristics is presented, for three values of reservoir thickness (h_{LC}). Starting from the nominal 3 µm case, the tolerance extrema are investigated. The variation of n_e tunes the extraordinary polarization wavelength within the active region gain window (830-850 nm, see Fig. 2). design aims to minimum threshold gain within this wavelength range. This is demonstrated by the red curves in Fig. 6 (a), where such minimum also corresponds to the middle of the possible n_e values (about 1.675). At the sides of this value, the threshold gain increases until it equals the value of the next longitudinal mode. This gives rise to a "sawtooth" behavior of the wavelength, whose height measures the FSR, 23 nm in our case.

Several longitudinal modes are supported by the structure (see Fig.3), but only that featuring the minimum 1D threshold gain is reported.

TABLE II
1D CROSS-SECTION OF THE ANALYZED STRUCTURE AT 850 nm.

Building Block	**Material**	**n**	**L [nm]**
Glass	HQ-Float Glass (PGO)	1.51	0.7×10^6
LC electrode	ITO	1.53-i0.007	45
7 pairs Top DBR	Ti_3O_5/SiO_2	2.13/1.45	100/147
Grating section	SU-8 2000	1.58	600
LC layer	QYDPLC-07 or -036	variable	3000
Current spreader	$Al_{0.15}GaAs$	3.513	497
Spacer	$Al_{0.8/0.25}GaAs$	3.10/3.43	20
Oxide aperture	$Al_{0.98}GaAs$	3	30
Spacer	$Al_{0.9}GaAs$	3.043	50
Grading	$Al_{0.35/0.55}GaAs$	3.37/3.24	90
barrier	$Al_{0.3}GaAs$	3.4	20
3QW active region	$Al_{0.3}GaAs/GaAs$	3.40/3.63	8/6
barrier	$Al_{0.3}GaAs$	3.4	20
Graing	$Al_{0.35/0.55}GaAs$	3.37/3.24	90
36.5 pairs Bottom DBR	$Al_{0.9/0.15}GaAs$	3.04/3.51	70/60.5
Substrate	GaAs	3.63	3×10^5

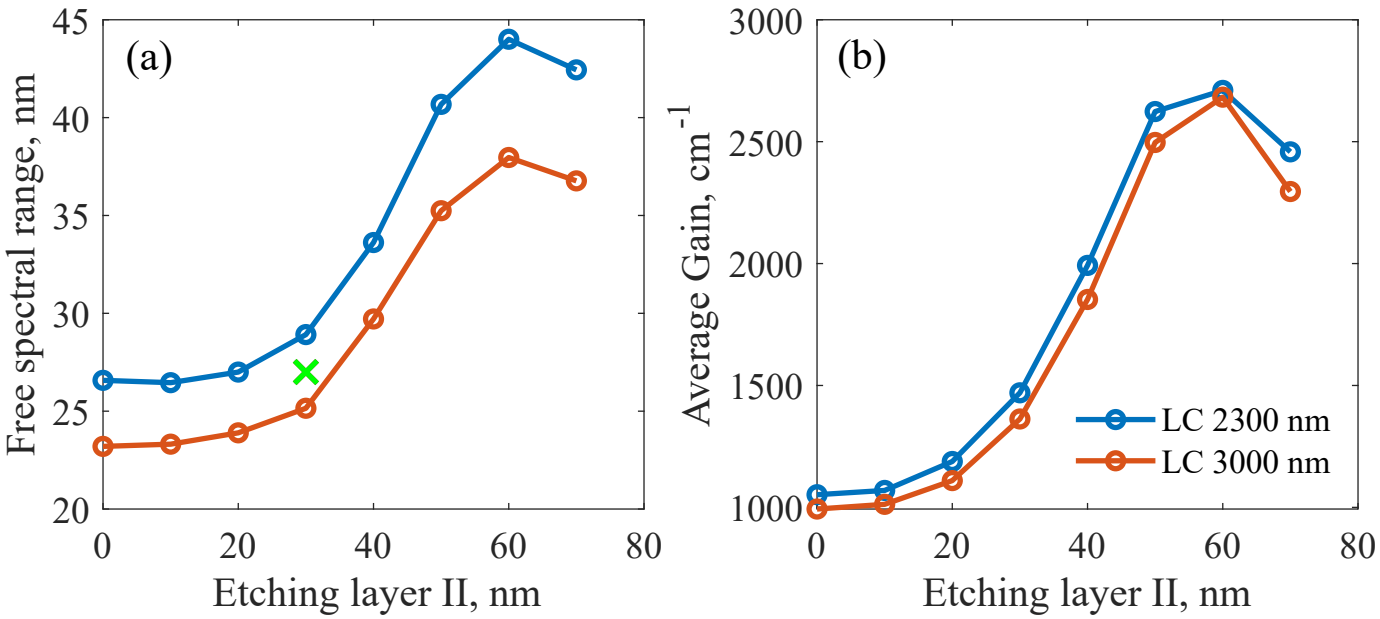

Fig. 5. (a): EM free spectral range and average (over n_e) gain for two LC thicknesses vs. etching thickness of the AlGaAs layer below the GaAs contact top layer. The green cross corresponds to the experimental value of Fig. 3. (b): corresponding average threshold gain. These curves are computed by 1D simulation where n_e is varied, as in Fig. 6.

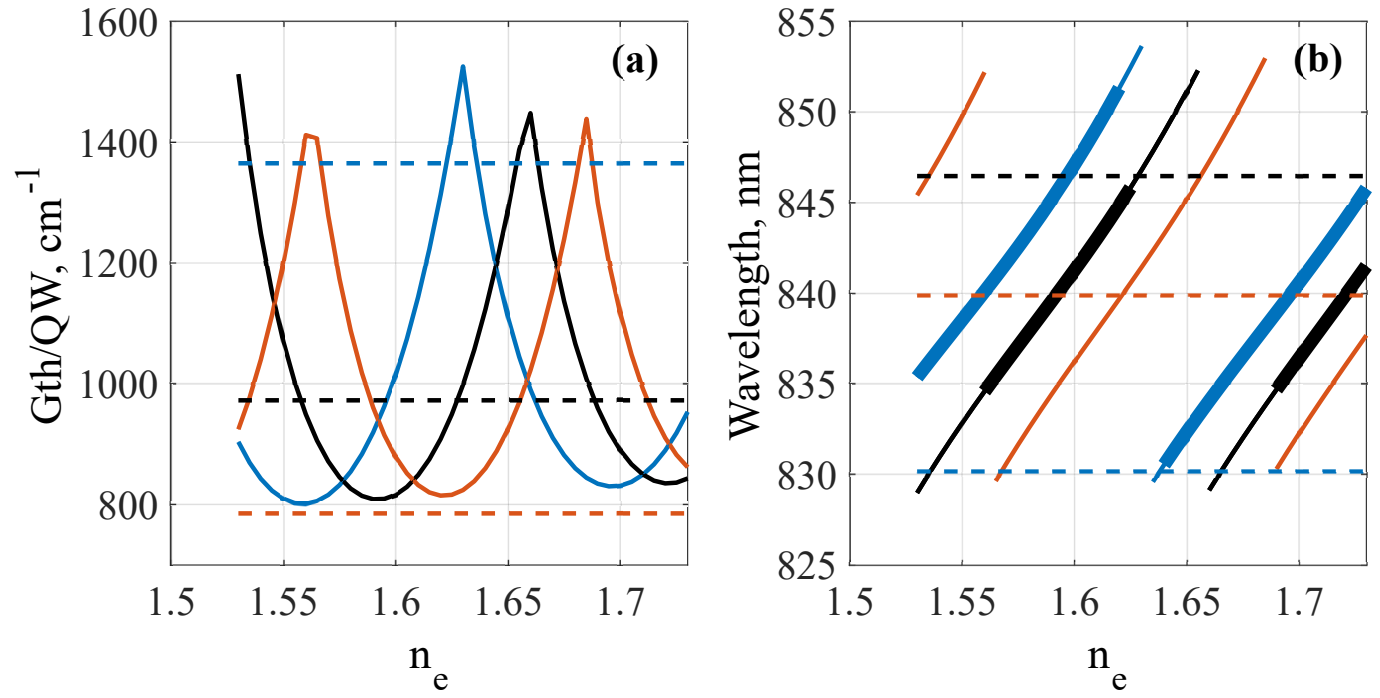

Fig. 6. 1D tuning performance (variation of n_e, while n_o is 1.51) for reservoir thicknesses of 2.8 (red), 3.0 (nominal design, in black) and 3.2 µm (blue). (a): threshold gains for extraordinary (continuous lines) and ordinary mode (dashed lines). (b): corresponding modal wavelengths; the thick lines correspond to extraordinary mode lasing.

C. Anisotropic transverse confinement design

Even if the tuning mechanism is based on the voltage-dependent n_e (extraordinary mode, EM), it is very important to monitor the corresponding ordinary polarization features (ordinary mode, OM, dashed lines). The EM threshold gain must be always lower than its ordinary counterpart, in order to guarantee an efficient tuning operation. The OM depends only on the geometrical lengths of the structure, being

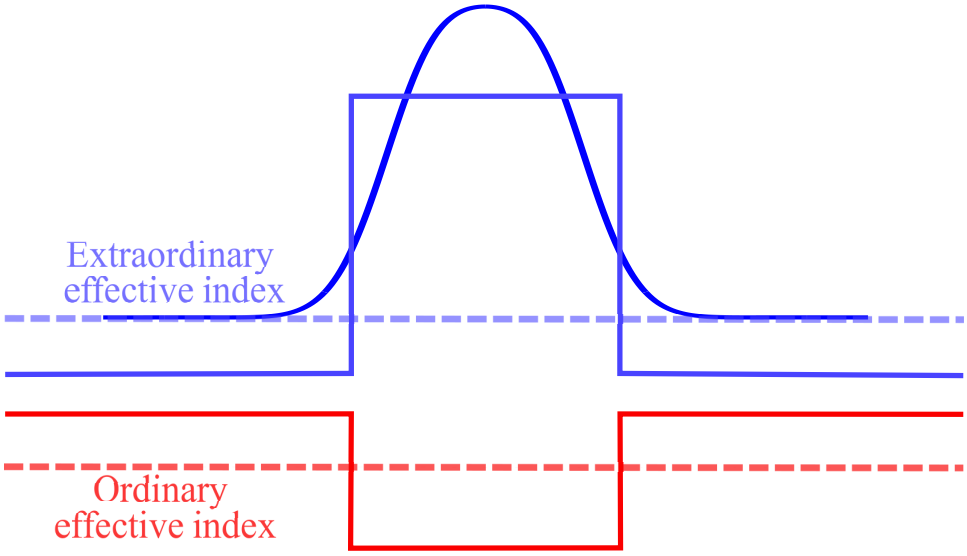

Fig. 7. Polarization-dependent (extraordinary in blue and ordinary in red) effective index scheme of the investigated structure. This method is not used in our work, but just deployed to illustrate the working principle of our design.

its ordinary index independent from the tuning voltage in a simple 1D picture. In this view, in Fig. 6(b) the wavelength tuning curves are rendered with two different thicknesses: where the line is thin, the OM is lasing and no tuning can be achieved. EM operation, indicated by thick lines, is either limited or absent, depending on the reservoir thickness uncertainties. For h_{LC} = 3.2 µm, the EM dominates, as desired. However, there exists also an opposite case (red curve), where the device would not work, emitting always on the OM. That makes clear that we need countermeasures to ensure EM lasing for any possible LC index and thickness.

In our structure, the alignment grating cannot select the EM, due to its too weak index contrast (1.58 for SU-8 against 1.51 to 1.72 for LC). A much stronger effect would occur with a grating positioned at the semiconductor-LC interface. However, 1D investigations (not reported in this work) show that even such stronger dichroism is not sufficient to counteract the large phase effects introduced by the tolerances of our technology. Moreover, the smaller grating area (at the mesa surface, corresponding to the $w_{\mathrm{SiON\,AG\,inner}}$ in Fig. 1) would lead to a less uniform LC alignment in the microcell.

Two ways could lead to EM always dominating:

1) a high-contrast grating (HCG) as top mirror;
2) transverse confinement engineering.

We opt for the second option, because HCGs are technologically challenging objects [30], [4], [31], [21], [29].

We propose here for the first time a design which we call anisotropic transverse confinement. It is based on the fact that $n_o < n_e$. Thinking in terms of the transverse effective index method [32], the sketch of Fig. 7 can be drawn. The outer effective index value can be engineered by modifying the composition of the passivation layer. In fact, the refractive index of this ternary dielectric material can be designed between that of SiO_2 (n = 1.45) and of Si_3N_4 (n = 2) by selecting an adequate composition during its deposition. If the index of the SiON is designed to be at 1.56 (recalling that $n_o \simeq 1.51$), one would achieve the effective transverse index profile depicted in Fig. 7. For voltages such that $n_e \geq 1.57$, the extraordinary polarization is guided, while the ordinary mode experiences antiguiding and will stay suppressed. The 1 µm thick dielectric SiON ring ensures proper operation: OM antiguiding (suppression) and EM guiding. This design is at almost zero cost, because it exploits the existing passivation layer, which anyway is needed for electrical insulation.

The only way to verify this innovative design is to run a full electro-thermo-optical simulation, as presented in the next section.

IV. Electrically Pumped LC-VCSEL Simulation

The LC-VCSEL performance, beside the usual VCSEL entangled interactions, critically depends on the antiguiding thermal features of the liquid crystal, which also differ among the different available types. To quantitatively access them, we applied VENUS, our comprehensive VCSEL suite [23], [33]. Here, major modifications were undertaken, in view of the hybrid LC-VCSEL under analyses, where thermal, optical and electrical regions have a completely different alignments compared to standard devices. For the half-VCSEL electro-thermal parameters, all details can be found elsewhere [33].

In Fig. 8, for different values of n_e, we report macroscopic results, such as VI and corresponding differential resistance, optical output power, SMSR, and tunability vs. current. The maximum inner temperature is the only quantity not directly measurable. They refer to a 4 µm oxide aperture device and the nominal values of the organic layers (see Table I and II). It features good SM optical power, which are favored by the extended cavity length [34]. At 6 mA it varies from 2 to 5 mW, related to wavelength, as already observed in previous cases [1].

The tuning range can be determined as 22 nm at the switching current of 1.8 mA for n_e=1.66 (green curve), in correspondence of the longitudinal mode hopping. The wavelengths reported in Fig. 8 (and similar ones in following figures) refer to the highest emitted modal power, which does not mean that other modes do not contribute to laser action, as specified by the SMSR. Threshold is moderate and it varies from 0.4 to 0.6 mA depending on n_e (see Fig. 6).

The changing slopes of the tuning wavelengths vs. current is due to antiguiding, which is maximum for the highest n_e. Therefore, we observe that for high n_e values the antiguiding dominates, causing a wavelength blue shift. For low n_e values we retrieve the normal red shift (blue and magenta curves, n_e=1.57 and 1.72). For n_e=1.6 we observe an almost perfect balance between the two effects.

A. Thermal Effects

Before moving to any detail of vectorial optical simulations, it is fundamental to analyze thermal effects. In fact, the situation sketched in Fig. 7 results from delicate balances between guiding and antiguiding phenomena, which can be modified by QW active response and, especially, thermal profiles.

Fig. 9 shows details of the thermal features at operation current of 5 mA: discontinuous thermal conductivities, temperature map and, below, more quantitative longitudinal and radial cuts. They show how the low LC thermal conductivity results in a sharp temperature decrease in the LC. It drops from the peak value, attained in the active region/spreading layer next to the LC, to almost the ambient value (always assumed in this work 300 K) in the glass substrate, supporting the top-DBR. Radially, the temperature drop resembles a Gaussian profile that scales with the oxide aperture, at least in the central and optically most important region.

The temperature profile in standard VCSELs causes a guiding effect, which enhances higher modes lasing at increases pumping. In LC-VCSELs all is complicated by the blended guiding/antiguiding features of the semiconductor/LC sections. The derivative with respect to temperature of the refractive index, $\mathrm{d}n/\mathrm{d}T$, causes the red shift observed in standard VCSEL under increasing current. In LCs is estimated to -2.1×10^{-3} (LC type 1) and $-1.3 \times 10^{-3}\,\mathrm{K}^{-1}$ (LC type 2), [26], [27] , i.e., about 10 times larger, in absolute value, than the value for the half-VCSEL ($2.4 \times 10^{-4}\,\mathrm{K}^{-1}$, [33]). Therefore, the temperature distribution induces a focusing index profile in the half-VCSEL and a defocusing one in the LC reservoir, in competition between them. These phenomena are mentioned in [12] and their coupling with electrical injection in the half-VCSEL is studied in details for the first time in this work, to the best of our knowledge.

To appreciate the relevance of this effect, in Fig. 10 we compare the two considered LCs and also artificially drop any LC temperature dependence. In this way, by eliminating the related LC antiguiding, we can better discuss its impact on the overall performance. The characteristics mostly coincide for low pump levels (say up to 1 mA), where thermal effects are very weak. In Fig. 10 we report the quantities mostly affected by the present investigation: LI, SMSR and wavelength variation vs. current, keeping in mind that temperature profiles are nearly equal in the three cases. For Type 1 LC the clearing temperature

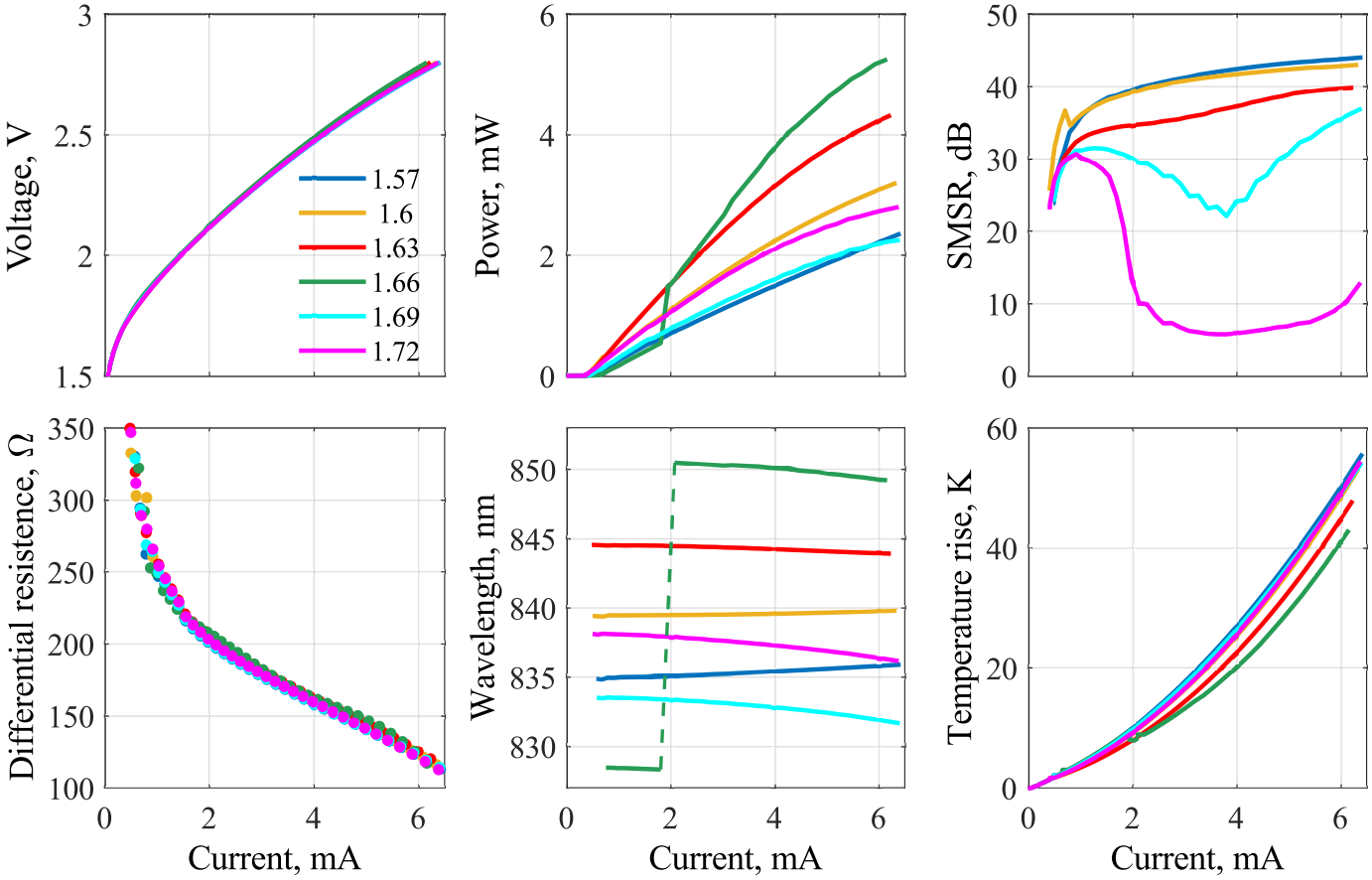

Fig. 8. Tuning performance (n_e, see legend) for VI, LI, SMSR, differential resistance, lasing wavelength and peak temperature. A 4 µm oxide apertures, 3 µm reservoir at 600 nm SU-8 are considered, with an ambient temperature of 300 K.

is reached much earlier (at about 4.5 mA), and operation ends at that current, resulting therefore into a reduced maximum output power. The reduction of LC index with temperature, induces a reduction of the lasing wavelength at increasing temperature, the opposite compared to standard VCSELs. When setting to zero the antiguiding (blue curves), the standard wavelength increase is recovered: about 1.5 nm in 6 mA, lower than normal, because of the dielectric top-DBR. The LC with lower clearing temperature features the highest $\mathrm{d}n/\mathrm{d}T$ coefficient, which leads to an inverted wavelength dependence vs. current: blue-shift instead of red-shift. Type 2 LC roughly compensates for the thermal lensing of the half-VCSEL so that the wavelength reduction over the whole operation range is just 0.5 nm in this example.

The impact of LC antiguiding clearly appear also in the LI curves: stronger antiguiding means higher modal losses, and therefore less output optical power. Antiguiding is however beneficial to SMSR, which increases with current in an LC-VCSEL, as opposed to standard VCSELs. The here quantified superior performance of Type 2 LC, directly connected to its higher clearing temperature, selects it as a better choice LC for tunable VCSELs.

B. Fully Vectorial Optical Simulation

We can now investigate the impact of the anisotropic transverse confinement design with VELM [20], by deploying its spatially dependent anisotropic capabilities [36]. The LC refractive index is treated as a tensor, and each field component feels the proper index. Our structure is computationally challenging. In fact, the presence of radiation losses mechanisms, previously analyzed in [37], did not include in-cavity metals (contact ring and Al contact-pad). Such unusual feature required a major VELM update. The standard approach of using generalized transmission matrices incurs into numerical problems when large

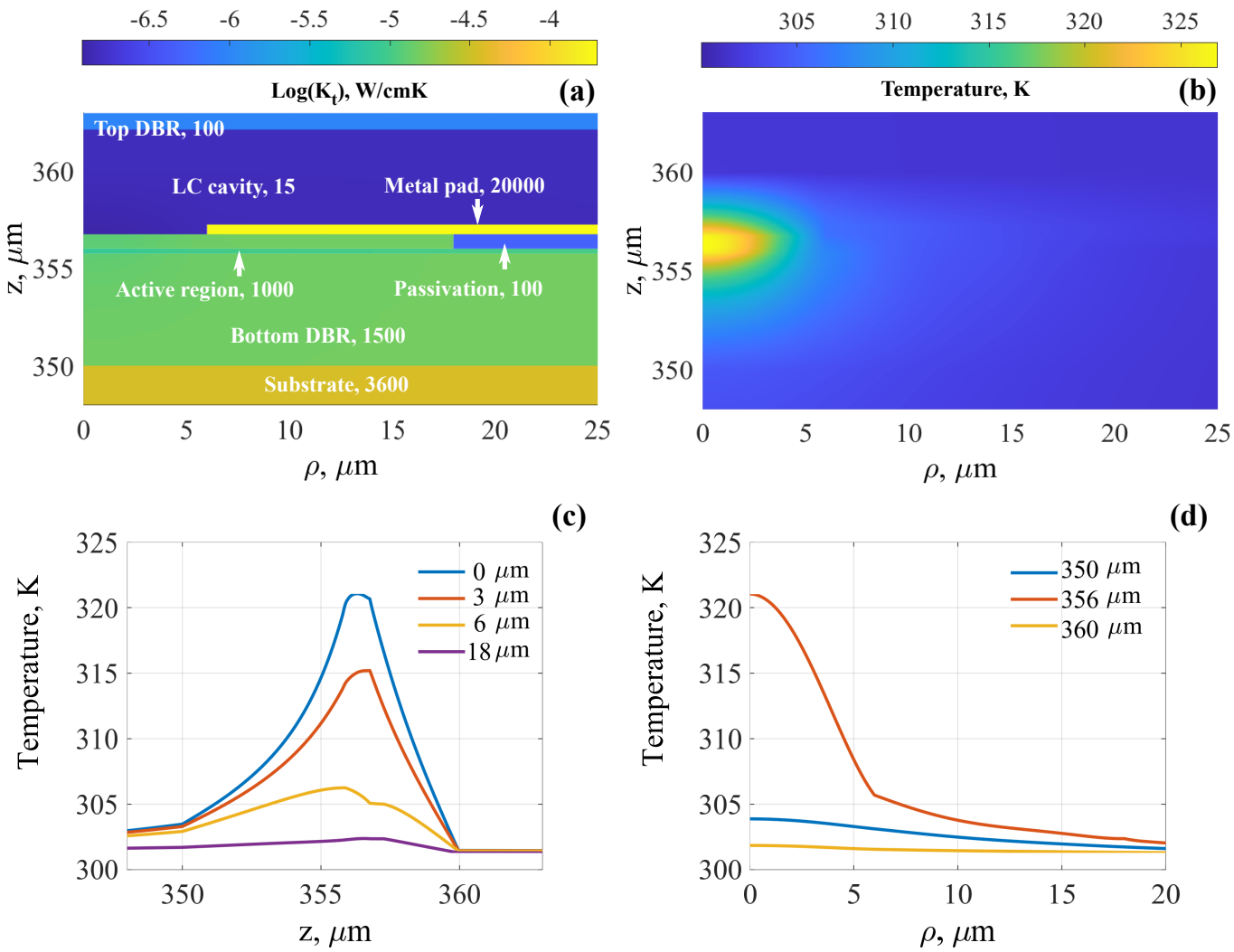

Fig. 9. (a) Map of the thermal conductivity (ρ-z cut) and (b) corresponding thermal profile for a 4 µm VCSEL with n_e = 1.63 and I=5 mA around the active region. Thermal conductivity values (in W/cmK) are indicated by white labels, on the (a) map where the different regions are identified. For semiconductor see [33], for glass, top-DBR and for LC see [35]. (c) longitudinal temperature cuts at different radii (see legend); (d) transverse temperature cuts at different longitudinal sections. z=0 correspond to the heatsink, below the 350 µm substrate.

imaginary parts of thick layers come into play, as for the 500 nm thick Al-pad, which covers most of the half VCSEL periphery. Therefore, a dedicated scattering matrix treatment was implemented, robust against any kind of imaginary part and thickness of the layers. The large spread of transverse dimensions (from 200 nm of the grating period, to 50 µm of the metal pad diameter), requires a modal expansion set much larger than usual [23]. The temperature profile, strongly varying in each device region, does not allow any computation shortcut (not even in the DBR), and anisotropies imply azimuthal mode coupling, so that at least two azimuthal orders must be included [20].

For sake of brevity, here we report a investigation of the tuning performance of the optimal device, including its robustness against technological tolerances. In Fig. 11 we show four panels that summarize our results, to be closely compared with Fig. 6. It demonstrates that our transverse design guarantees EM lasing by preserving the same tuning features. Threshold gain plot (a) reports the transverse modes of interest: fundamental EM, fundamental OM and first order EM. By comparing 1D and 3D gains, only fundamental EM displays the typical nearly-periodic gain variation vs. n_e. Its threshold gain is slightly higher than in the 1D model due to the various transverse features but stays mostly below 2000 cm^{-1} and therefore it is fully sustainable by our QWs (see Fig. 2). Instead, fundamental OM is highly suppressed by its large losses (nearly ten times higher, which corresponds to a dichroism always larger than 70%).

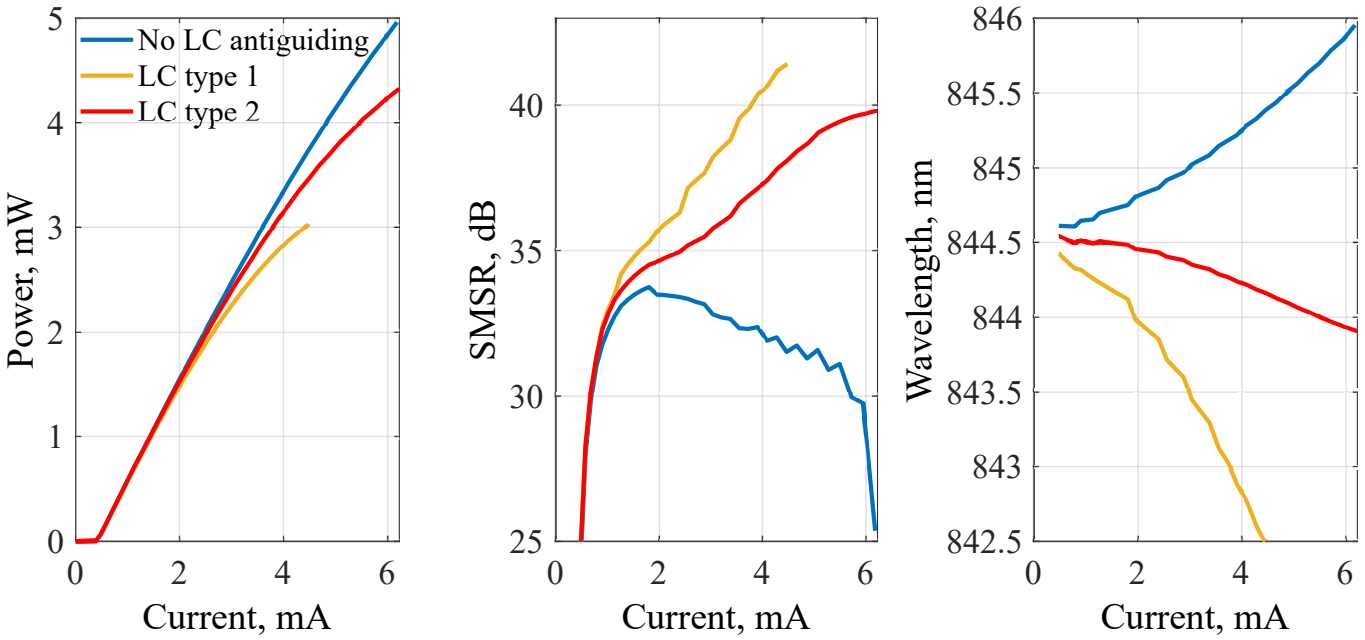

Fig. 10. LC-VCSEL performance vs. LC antiguiding features: LI, SMSR and lasing wavelength for a 4 µm oxide aperture, n_e=1.63, 3 µm reservoir, 600 nm SU-8 and ambient temperature of 300 K.

Contrary to the 1D approach, VELM shows its clear dependence on n_e, due to the vector features of the VCSEL modes. Being FOM less confined than FM, when n_e value approaches the n_{SiON} one (becoming less localized) its losses strongly increase. Therefore, the corresponding dichroism (d, see also caption of Fig. 11) is good in that regime, while it becomes poorer at high n_e values. Here, we want to explore both the uncertainties on organic layers thicknesses (three values of h_{LC} and three of $h_{\mathrm{SU-8}}$, nine structures on total), which result in very dense plots. What is important to obtain from Fig. 11 is not the single detail, but the overall compliance of our design to the specs.

The tuning features are summarized in Fig. 11-b and correspond well to the 1D model. Their reduction compared to 23-24 nm range achieved by VELM-1D is due to a coarser sampling of n_e (0.02). On the other hand, 3D simulations are mandatory for transverse mode analysis. In summary, while free spectral range and EM tuning are well and easily described by 1D models, the actual modal features requires a full vectorial and self consistent approach. In fact, most applications require stable SM emission, and therefore investigation of the FOM is of the highest importance. In Fig. 11 one can see that fundamental EM operation is guaranted for low n_e, where the guiding is weaker and FOM much less confined that FM. However, for high n_e the gain difference is small (approaching 0 in some cases). This explains the SMSR result plot of Fig. 8 where we can see that the standard 30 dB criterion for SM operation is lost for some of the tuning values.

C. Oxide Aperture and Single Mode Features

We can now discuss the last critical parameter of our device, which rules its SM features: the oxide aperture diameter. As discussed earlier, most applications require single fundamental mode operation. To hit this goal, we tested several solutions, such as applying a diffractive optical element [37], using a simple relief in the last semiconductor layer [38] or playing with the etching size of the GaAs cap layer. The first two approaches did not prove to be robust for SM operation, while a smaller GaAs etching would increase also the threshold gain of the FM. Therefore, we still relay on the usual approach of a small oxide aperture [39].

Fig. 12 shows the major impacts of the oxide aperture on all the relevant characteristics: electrical, thermal and optical. Larger apertures enable higher currents at equal applied voltages. The differential

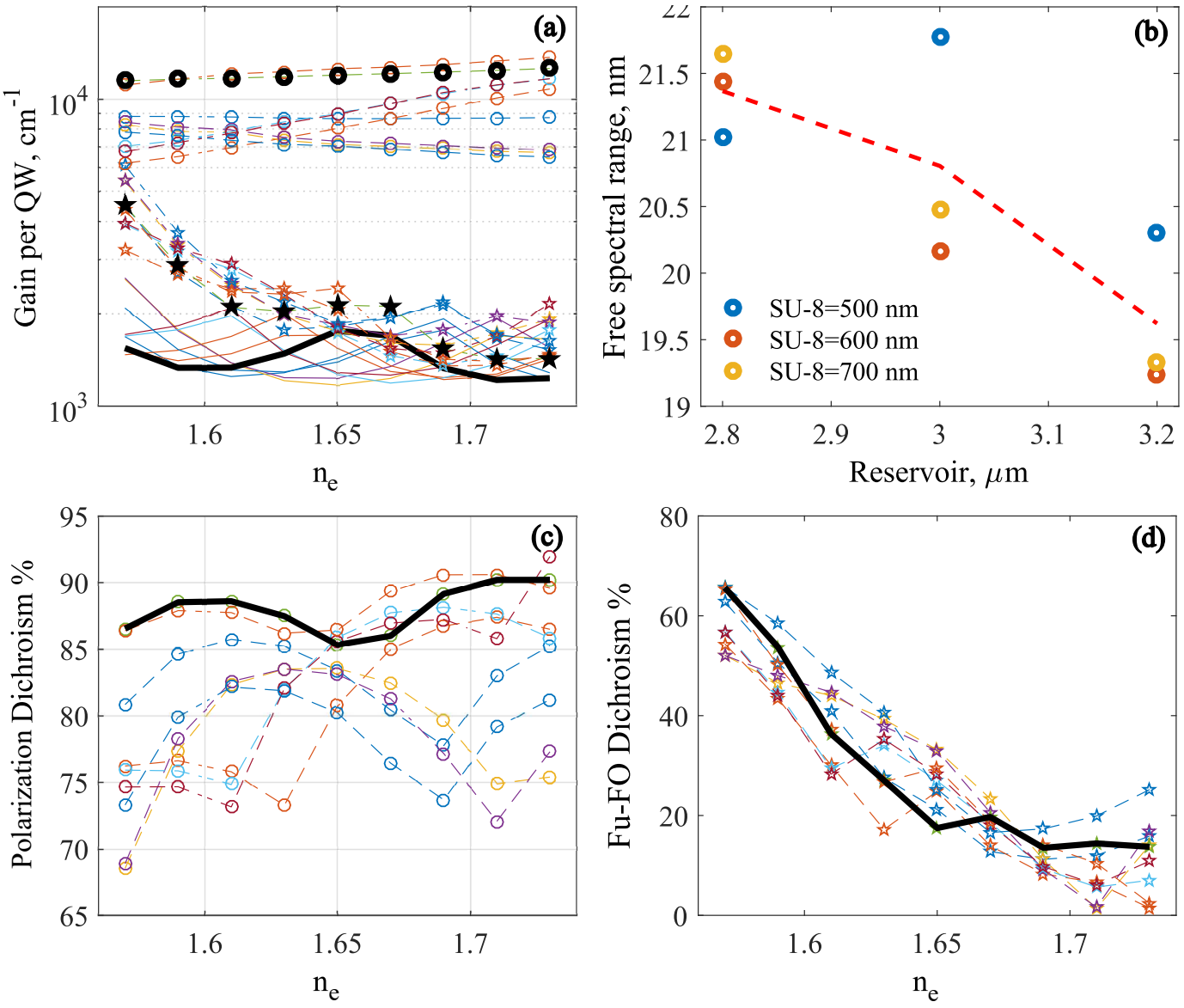

Fig. 11. Tuning performance (n_e variation, plots a-c-d) at injection current of 5 mA for the 4 μm oxide aperture; the nine investigated structures refer to the tolerance of reservoir (3.0 ± 0.2) μm and SU-8 (600 ± 100) nm; in black, the nominal design. (a): modal losses for fundamental EM (continuous lines), fundamental OM (circles) and first order EM (stars). (c): polarization dichroism (1-G_{EM}/G_{OM}). (d): dichroism, defined similarly to (c) but for G_{EM} and its corresponding first order mode. (b): free spectral range vs reservoir tolerance.

resistance is inversely proportional to oxide aperture just for low currents; this trend changes at about 6 mA, which is, however, the maximum suggested value for proper LC operation (temperature issues). The higher modal losses of smaller apertures are in part compensated by the stronger injection needed to achieve the same current density for larger apertures. Therefore, the threshold current just scales linearly with the aperture, instead of quadratically (from 0.4 to 0.6 mA). As a consequence, LI curves are almost superimposed. However, the real problem in a tunable VCSEL is to keep a high SMSR for the whole tuning range. For a 5 μm aperture, FM operation is rapidly lost in favor of a double emission, with a predominant contribution of the FOM. This is the reason of the 1 nm wavelength jump (red curve, middle plot of Fig. 12), which indicated the injection where the FOM becomes dominant.

Discarding a 5 μm oxide aperture, due to its non-compliance to SM operation, it becomes relevant to investigate the performance of 3 μm device, reported in Fig. 13 and to be compared with Fig. 8. For n_e =1.66 we recover a similar wavelength switching, at slightly anticipated current of 1.4 mA, due to earlier

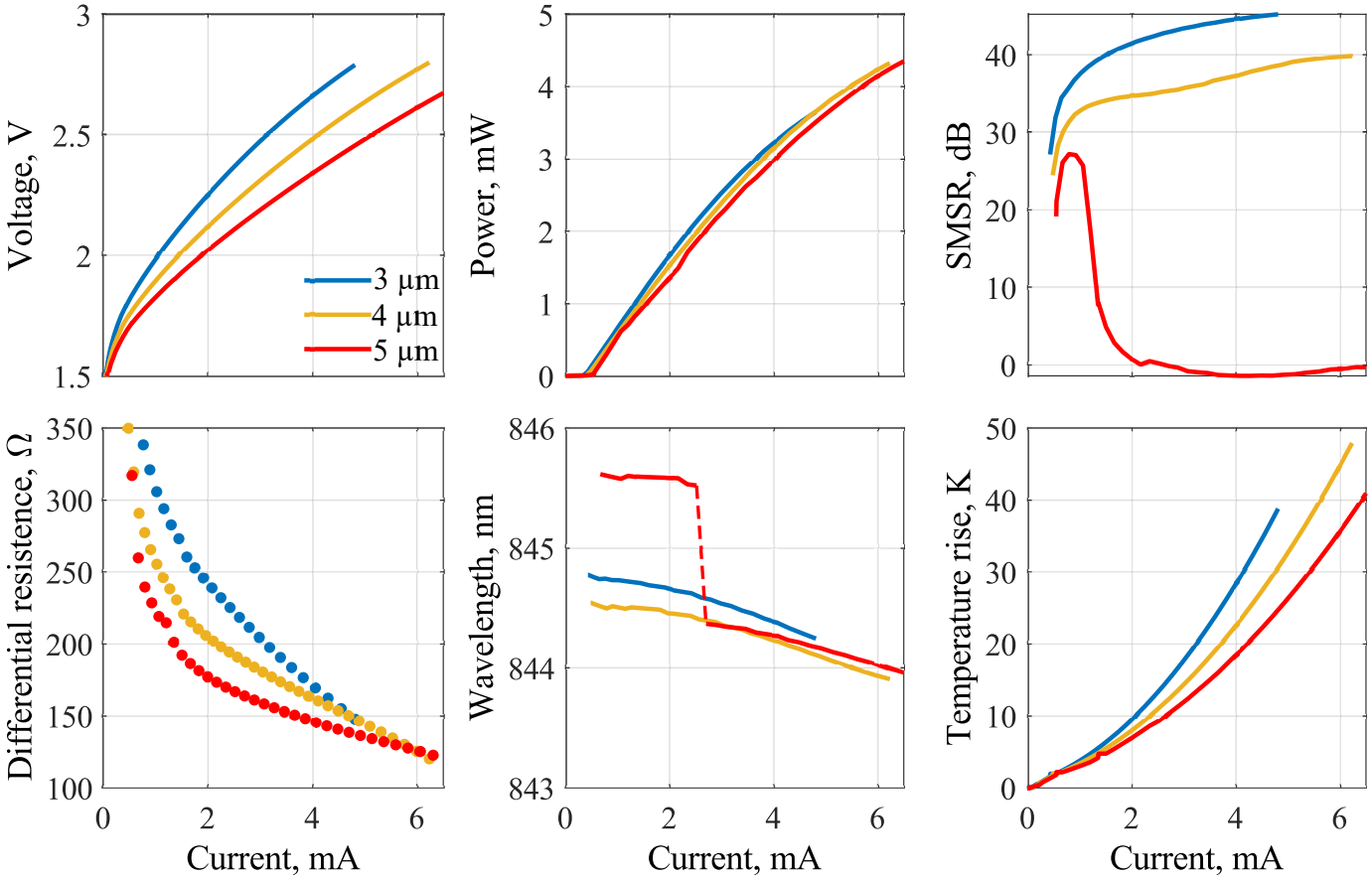

Fig. 12. LC-VSCEL characteristics vs. oxide aperture (see legend) for n_e = 1.63.

self-heating. Maximum temperature depends mildly on the tuning position: when output power is higher (blue curves), less optical free-carrier absorption (heat) develops in the half-VCSEL. SMSR exceeds 40 dB above 2 mA, for all tuning conditions. This confirms 3 µm as the best oxide aperture to be targeted, with the usual ±0.5 µm tolerance being acceptable.

V. Conclusion

A 850 nm electrically-driven tunable LC-VCSEL based on a new polymer microcell technology, recently proven in an optical pumping configuration, is investigated and optimized. The interplay of thermal, electrical and optical phenomena is investigated in depth, to identify a design that guarantees single fundamental mode operation, tuned through 23 nm at room temperature in continuous wave regime. This is a challenging task, especially for the large uncertainties on the thicknesses of the organic layers used for the LC microcell, where the LC molecules are aligned by a nanoimprinted grating. The 23 nm tuning range is a consequence of our conservative design, aiming for the smallest threshold rather than for the highest free spectral range (44 nm).

To guarantee laser action only for the fundamental OM, we propose here for the first time a dichroic transverse guiding design, based on a dielectric ring, with properly designed refractive index. This ring, derived from the passivation layer deposited on the half-VCSEL surface, is proven effective in all working conditions and might be applied to LC-VCSELs operating at other wavelengths. We also demonstrate the many advantages of using a nematic LC featuring a higher clearing temperature (95 °C) than standard E7 LC: better transverse confinement (reduced antiguiding in the LC reservoir) and higher output power, due to higher possible temperature rise. The half-VCSEL part was also optimized as for its oxide aperture diameter, to ensure good SMSR over the whole operation range: a 3 µm aperture ensures 40 dB SMSR

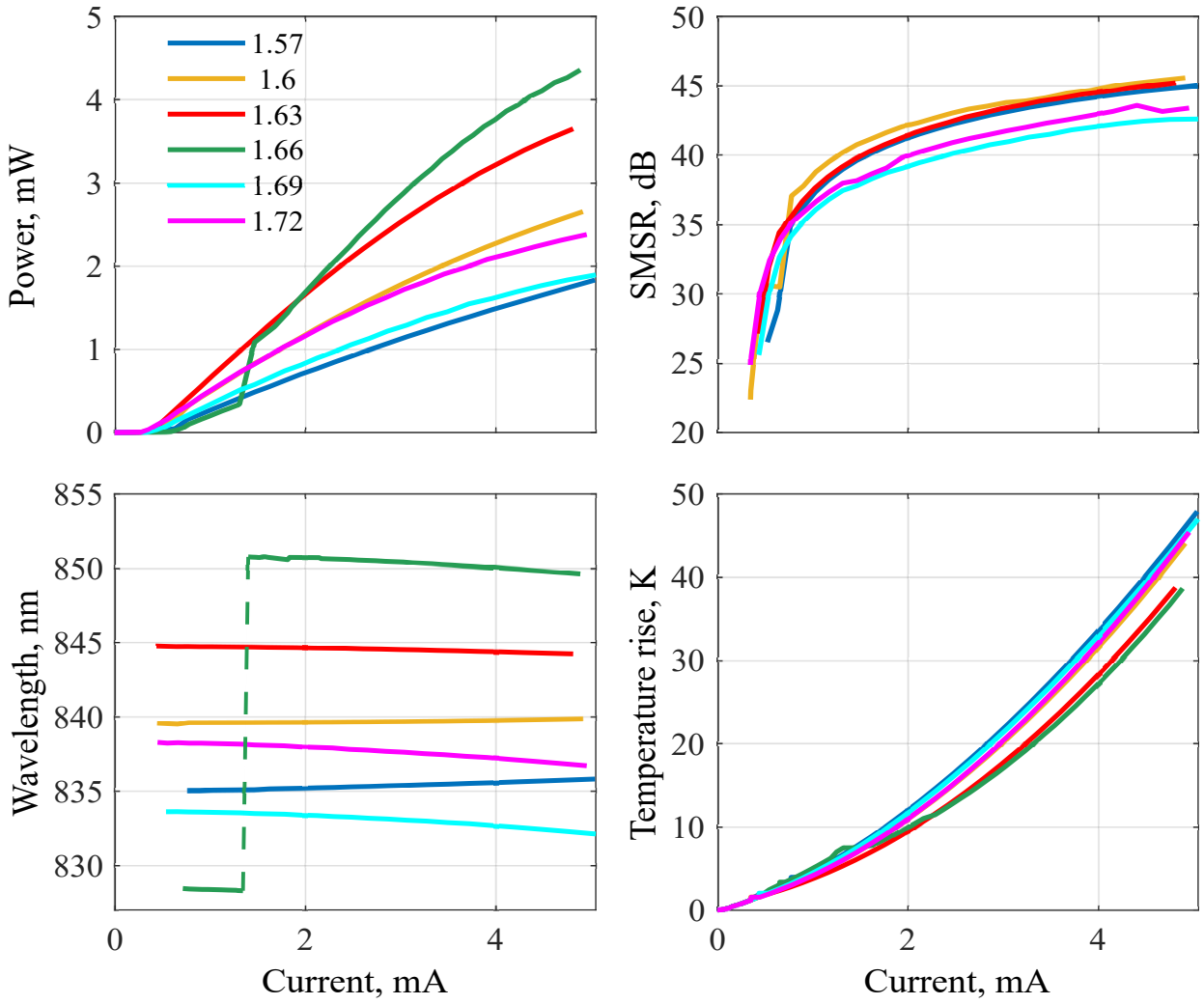

Fig. 13. Tuning performance (n_e legend) of a 3 µm oxide aperture LC-VCSEL. 3 µm reservoir and 600 nm SU-8 are considered, with an ambient temperature of 300 K.

in all conditions and optical power in the 2-4 mW range. These results will be exploited to reach a first demonstration of electrically-driven LC tunable VCSELs.

ACKNOWLEDGMENTS

This work was supported by Agence Nationale de la Recherche (ANR) (grant number:ANR-15-CE19-0012 DOCT-VCSEL). The authors acknowledge Pr. Laurent Dupont at IMT Atlantique, Brest, France for fruitful discussions and RENATECH (French Network of Major Technology Centers) for technical support.

REFERENCES

[1] C. Gierl, T. Gruendl, P. Debernardi, K. Zogal, C. Grasse, H. A. Davani, G. Böhm, S. Jatta, F. Küppers, P. Meißner, and M.-C. Amann, "Surface micromachined tunable 1.55 μm-VCSEL with 102 nm continuous single-mode tuning," *Opt. Express*, vol. 19, no. 18, pp. 17 336–17 343, Aug. 2011.

[2] P. Qiao, K. Cook, K. Li, and C. Chang-Hasnain, "Wavelength-swept VCSELs," *IEEE J. Select. Topics Quantum Electron.*, vol. 23, no. 6, p. 1700516, 2017.

[3] B. Kogel, P. Debernardi, P. Westbergh, J. S. Gustavsson, Å. Haglund, E. Haglund, J. Bengtsson, and A. Larsson, "Integrated mems-tunable VCSELs using a self-aligned reflow process," *IEEE J. Quantum Electron.*, vol. 48, no. 2, pp. 144–152, 2012.

[4] C. J. Chang-Hasnain and W. Yang, "High-contrast gratings for integrated optoelectronics," *Adv. Opt. Photonics*, vol. 4, no. 3, pp. 379–440, 2012.

[5] M. Fill, P. Debernardi, F. Felder, and H. Zogg, "Lead-chalcogenide mid-infrared vertical external cavity surface emitting lasers with improved threshold: Theory and experiment," *Appl. Phys. Lett.*, vol. 103, pp. 201 120–1–3, 2013.

[6] D. D. John, C. B. Burgner, B. Potsaid, M. E. Robertson, B. K. Lee, W. J. Choi, A. E. Cable, J. G. Fujimoto, and V. Jayaraman, "Wideband electrically pumped 1050-nm MEMS-tunable VCSEL for ophtalmic imaging," *J. Lightwave Technol.*, vol. 33, no. 16, pp. 3461–3468, 2015.

[7] D. D. John, B. Lee, B. Potsaid, A. C. Kennedy, M. E. Robertson, C. B. Burgner, A. E. Cable, J. G. Fujimoto, and V. Jayaraman, "Single-mode and high-speed 850nm MEMS-VCSEL," in *Lasers Congress 2016 (ASSL, LSC, LAC)*. Optical Society of America, 2016, p. ATh5A.2.

[8] K. Panajotov, Y. Xie, M. Dems, C. Belmonte, H. Thienpont, J. Beeckman, and K. Neyts, "Vertical-cavity surface-emitting laser emitting circularly polarized light," *Laser Phys. Lett.*, vol. 10, no. 10, p. 105003, 2013.

[9] Y. Xie, J. Beeckman, K. Panajotov, and K. Neyts, "Vertical-cavity surface-emitting laser with a liquid crystal external cavity," *Opt. Lett.*, vol. 39, no. 22, pp. 6494–6497, 2014.

[10] K. Panajotov, M. Dems, C. Belmonte, H. Thienpont, Y. Xie, J. Beeckman, and K. Neyts, "Vertical-cavity surface-emitting laser with cholesteric liquid crystal overlay," *J. Lightwave Technol.*, vol. 32, no. 1, pp. 20–26, 2014.

[11] C. Belmonte, L. Frasunkiewicz, T. Czyszanowski, H. Thienpont, J. Beeckman, K. Neyts, and K. Panajotov, "Optimization of electrically tunable VCSEL with intracavity nematic liquid crystal," *Opt. Express*, vol. 23, no. 12, pp. 15 706–15 715, 2015.

[12] L. Frasunkiewicz, T. Czyszanowski, H. Thienpont, and K. Panajotov, "Electrically tunable VCSEL with intra-cavity liquid crystal: Design, optimization, and analysis of polarization and mode-stability," *Opt. Commun.*, vol. 427, pp. 271–277, 2018.

[13] O. Castany, L. Dupont, A. Shuaib, J. P. Gauthier, C. Levallois, and C. Paranthoën, "Tunable semiconductor vertical-cavity surface-emitting laser with an intracavity liquid crystal layer," *Appl. Phys. Lett.*, vol. 98, no. 16, p. 161105, 2011.

[14] B. Boisnard, C. Levallois, C. Paranthoes, S. Pes, T. Camps, B. Sadani, K. Tavernier, S. Bouchoule, L. Dupont, M. Alouini, P. Debernardi, and V. Bardinal, "CW operation of a tunable 1550 nm VCSEL integrating liquid-crystal microcells," *IEEE Photon. Technol. Lett.*, vol. 32, no. 7, pp. 391–394, 2020.

[15] X. Li, V. Kozenkov, F. Yeung, P. Xu, V. Chigrinov, and H. Kwok, "Liquid-crystal photoalignment by super thin azo dye layer," *Japan. J. Appl. Phys.*, vol. 45, no. 1, pp. 203–205, 2006.

[16] A. V. Syrbu, J. Behrend, J. Fernandez, J. F. Carlin, C.-A. Berseth, V. P. Iakovlev, A. Rudra, and E. Kapon, "Thermal stability of InP-based structures for wafer fused laser diodes," *J. Cryst. Growth*, vol. 188, no. 1, pp. 338–342, 1998.

[17] B. Sadani, B. Boisnard, X. Lafosse, T. Camps, J. Doucet, E. Daran, C. Paranthoën, C. Levallois, L. Dupont, S. Bouchoule, and V. Bardinal, "Liquid-crystal alignment by a nanoimprinted grating for wafer-scale fabrication of tunable devices," *IEEE Photon. Technol. Lett.*, vol. 30, no. 15, pp. 1388–1391, 2018.

[18] C. Levallois, B. Sadani, B. Boisnard, T. Camps, C. Paranthoën, S. Pes, S. Bouchoule, L. Dupont, J.-B. Doucet, M. Alouini, and V. Bardinal, "Liquid crystal-based tunable photodetector operating in the telecom C-band," *Opt. Express*, vol. 26, no. 20, pp. 25 952–25 961, 2018.

[19] G. P. Bava, P. Debernardi, and L. Fratta, "Three-dimensional model for vectorial fields in vertical-cavity surface-emitting lasers," *Phys. Rev. A*, vol. 63, no. 2, p. 23816, 2001.

[20] P. Debernardi and G. P. Bava, "Coupled mode theory: a powerful tool for analyzing complex VCSELs and designing advanced devices features," *IEEE J. Select. Topics Quantum Electron.*, vol. 9, no. 3, pp. 905–917, 2003.

[21] A. Tibaldi, P. Debernardi, and R. Orta, "Bimodal resonance phenomena–part III: high-contrast grating reflectors," *IEEE J. Quantum Electron.*, vol. 54, no. 6, pp. 6 600 108–1–8, 2018.

[22] Pusch, T., Debernardi, P., Lindemann, M., Erb, F., Gerhardt, N.C., Hofmann, M.R., and R. Michalzik, "Vertical-cavity surface-emitting laser with integrated surface grating for high birefringence splitting," *Electron. Lett.*, vol. 55, no. 19, pp. 1055–1057, 2019.

[23] A. Tibaldi, F. Bertazzi, M. Goano, R. Michalzik, and P. Debernardi, "VENUS: a Vertical-cavity surface-emitting laser Electro-opto-thermal NUmerical Simulator," *IEEE J. Select. Topics Quantum Electron.*, vol. 25, no. 6, p. 1500212, Nov./Dec. 2019.

[24] M. Calciati, A. Tibaldi, F. Bertazzi, M. Goano, and P. Debernardi, "Many-valley electron transport in AlGaAs VCSELs," *Semiconductor Sci. Technol.*, vol. 32, no. 5, p. 055007, 2017.

[25] P. Debernardi, B. Kögel, K. Zogal, P. Meissner, M. Maute, M. Ortsiefer, G. Bohm, and M.-C. Amann, "Modal properties of long-wavelength tunable MEMS-VCSELs with curved mirrors: comparison of experiment and modeling," *IEEE J. Quantum Electron.*, vol. 44, no. 4, pp. 391–399, 2008.

[26] J. Li, S. Wu, S. Brugioni, R. Meucci, and S. Faetti, "Infrared refractive indices of liquid crystals," *J. Appl. Phys.*, vol. 97, no. 7, p. 073501, 2005.

[27] A. Simaz, B. Boisnard, T. Camps, J.-B. Doucet, B. Reig, A. Tibaldi, P. Debernardi, and V. Bardinal, "Thermal characterization of the birefringence of nematic liquid crystals for the design of widely-tunable LC-VCSELs," in *20th International Conference on Numerical Simulation of Optoelectronic Devices (NUSOD 2020)*, online, Sep. 2020, pp. 73–74.

[28] S.-T. Wu, "Molecular design strategies for high birefringence liquid crystals," in *MRS Proceedings*, vol. 709. Cambridge University Press, 2001, p. CC7.2.1.

[29] A. Tibaldi, P. Debernardi, and R. Orta, "High-contrast grating performance issues in tunable VCSELs," *IEEE J. Quantum Electron.*, vol. 51, no. 12, p. 2400407, 2015.

[30] C. F. R. Mateus, M. C. Y. Huang, Y. Deng, A. R. Neureuther, and C. J. Chang-Hasnain, "Ultrabroadband mirror using low-index cladded subwavelength grating," *IEEE Photon. Technol. Lett.*, vol. 16, no. 2, pp. 518–520, 2004.

[31] R. Orta, A. Tibaldi, and P. Debernardi, "Bimodal resonance phenomena–part I: generalized Fabry–Pérot interferometers," *IEEE J. Quantum Electron.*, vol. 52, no. 12, pp. 6 100 508–1–8, 2016.

[32] G. R. Hadley, "Effective index model for vertical-cavity surface-emitting lasers," *Opt. Lett.*, vol. 20, no. 13, pp. 1483–1485, 2005.

[33] P. Debernardi, A. Tibaldi, M. Daubenschüz, R. Michalzik, M. Goano, and F. Bertazzi, "Probing thermal effects in VCSELs by experiment-driven multiphysics modeling," *IEEE J. Select. Topics Quantum Electron.*, vol. 25, no. 6, p. 1700914, Nov./Dec. 2019.

[34] H. J. Unold, S. W. Z. Mahmoud, R. Jäger, M. Kicherer, M. C. Riedl, and K. J. Ebeling, "Improving single-mode VCSEL performance by introducing a long monolithic cavity," *IEEE Photon. Technol. Lett.*, vol. 12, no. 8, pp. 939–941, 2000.

[35] O. D. Lavrentovich, Y.-K. Kim, and B. I. Senyuk, "Optical manifestation of thermal expansion of a nematic liquid crystal," in *Proc. SPIE 8475*, Mar. 2012, p. 84750G.

[36] P. Debernardi and G. P. Bava, "Effects of anisotropies on vectorial modes of vertical-cavity surface-emitting lasers," *Phys. Status Solidi A*, vol. 188, no. 3, pp. 967–977, 2001.

[37] P. Debernardi and R. Orta, "Mastering lateral radiation losses in tunable VCSELs," *IEEE J. Quantum Electron.*, vol. 55, no. 1, p. 2400108, 2019.

[38] P. Debernardi, "HOT-VELM: a comprehensive and efficient code for fully vectorial and 3-D hot-cavity VCSEL simulation," *IEEE J. Quantum Electron.*, vol. 45, no. 8, pp. 979–992, 2009.

[39] P. Bienstman, R. Baets, J. Vukusic, A. Larsson, M. J. Noble, M. Brunner, K. Gulden, P. Debernardi, L. Fratta, G. P. Bava, H. Wenzel, B. Klein, O. Conradi, R. Pregla, S. A. Riyopoulos, J.-F. P. Seurin, and S. L. Chuang, "Comparison of optical VCSEL models on the simulation of oxide-confined devices," *IEEE J. Quantum Electron.*, vol. 37, no. 12, pp. 1618–1631, 2001.